energies

MDPI

Article

Heteroatom-Doped Nickel Sulfide for Efficient Electrochemical Oxygen Evolution Reaction

Xingqun Zheng [1,2], Ling Zhang [2], Wei He [3], Li Li [2,*] and Shun Lu [4,5,*]

[1] College of Safety Engineering, Chongqing University of Science & Technology, Chongqing 401331, China
[2] State Key Laboratory of Power Transmission Equipment & System Security and New Technology, College of Chemistry and Chemical Engineering, Chongqing Univerisity, Chongqing 400044, China
[3] Department of Electrical Engineering and Computer Science, South Dakota State University, Brookings, SD 57007, USA
[4] Department of Agricultural Engineering, South Dakota State University, Brookings, SD 57007, USA
[5] Chongqing Institute of Green and Intelligent Technology, Chinese Academy of Sciences, Chongqing 400714, China
* Correspondence: liliracial@cqu.edu.cn (L.L.); shun.lu@sdstate.edu (S.L.)

Abstract: Heteroatom doping is an effective strategy to regulate electrocatalysts for the oxygen evolution reaction (OER). Nonmetal heteroatoms can effectively engineer geometric and electronic structures and activating surface sites of catalysts due to their unique radius and the electronegativity of nonmetal atoms. Hence, the surface geometric and electronic structure and activity of nonmetal atoms (X, X = B, C, N, O, P)-doped Ni_3S_2 (X-Ni_3S_2) were studied to screen high-performance Ni_3S_2-based OER electrocatalysts through density functional theory calculation. Theoretical results demonstrated that dopants in X-Ni_3S_2 can alter bond length and charge of surface, modify active sites for intermediates adsorption, and adjust the theoretical overpotential. Among all dopants, C can effectively modulate surface structure, activate surface sites, weaken the adsorption of key intermediates, decrease theoretical overpotential, and enable C-Ni_3S_2 with the best theoretical OER activity among all X-Ni_3S_2 with the lowest theoretical overpotential (0.46 eV). Further experimental results verified that the synthesized C-Ni_3S_2 performed an improved OER activity in the alkaline condition with a considerably enhanced overpotential of 261 mV at 10 mA cm^{-2} as well as a Tafel slope of 95 mV dec^{-1} compared to pristine Ni_3S_2.

Keywords: heteroatom doping; oxygen evolution reaction; nickel sulfide; DFT calculations

Citation: Zheng, X.; Zhang, L.; He, W.; Li, L.; Lu, S. Heteroatom-Doped Nickel Sulfide for Efficient Electrochemical Oxygen Evolution Reaction. *Energies* **2023**, *16*, 881. https://doi.org/10.3390/en16020881

Academic Editors: Adriano Sacco and Mario Aparicio

Received: 13 November 2022
Revised: 1 December 2022
Accepted: 10 January 2023
Published: 12 January 2023

1. Introduction

Electrochemical water splitting is identified as a promising technology for renewable energy conversion [1,2]. Due to the relatively high energy barrier and the inertia involved in the four electron processes, the oxygen evolution reaction (OER), the anode reaction of water splitting exhibits slow kinetics, large reaction overpotential, and high energy consumption, which impede the efficiency of the hydrogen evolution reaction (HER) on the cathode of water splitting. Efficient electrocatalysts are crucial for facilitating the sluggish and energy-intensive OER. Up to now, Ru- and Ir-based oxides are the most prevalent and efficient catalysts for OER [3]. However, their inadequacy and high cost stymie their large-scale commercial applications. Therefore, designing highly active, durable, and nonprecious materials as alternative OER electrocatalysts is the key to overcoming the technical obstacles of hydrogen production and an intensively challenge for extensive commercial application of water splitting technology [4–6].

Ni-based nonprecious materials, such as sulfides [7–9], nitrides [10,11], oxides [12,13], and phosphides [9,14], have been extensively explored for OER in recent years. Among them, Ni_3S_2 has been regarded as a latent catalyst to replace Ru- and Ir-based noble OER catalysts due to its facile synthesis and inherent metal Ni–Ni connecting network, giving

it decent conductivity and praiseworthy catalytic activity. Nevertheless, the intrinsic activity of Ni_3S_2 is still inferior to the Ru and Ir oxides catalysts [15]. Strategies such as heteroatom doping, heterojunction, and morphology engineering have been devoted to promote the OER performance of catalysts [16]. Among these, heteroatom doping serves as an extremely effective method, and has been widely used to tune the structure and catalytic activity of Ni_3S_2. For example, introducing transition metal atoms (Fe, Co, Mn, V, etc.) into the catalysts' lattice can change lattice structure [8,16], modulate electronic structure [17,18], as well as increase the number of active sites [19,20] of catalysts resulting in improved catalytic activities for Ni_3S_2 materials. Similar to metal heteroatom regulation, nonmetal heteroatoms can also engineer geometric and electronic structures and activate surface sites of catalysts. Moreover, as the radius and electronegativity of nonmetal atoms (especially the second and third period nonmetal atom) usually differ greatly from that of transition-metal atoms, nonmetal atoms are more likely bringing about changes in the local coordinate environment and cause changes in the local geometric and electronic structures of active sites of catalysts [21]. This makes nonmetal heteroatoms more attractive in adjusting the electrocatalytic activity of materials. For example, the N heteroatom can significantly modify the electronic structure and morphology of Ni_3S_2, which brings high exposure of active sites, enhances conductivity, and optimizes HER activity [22]. Previous studies also proved that some nonmetal atoms (X, such as O, C, N) can adjust the electronic structure and increase the number of active sites in terms of HER study [23,24]. In this regard, nonmetal doping would be a more promising way to regulate the electronic structure and OER activity of Ni_3S_2. Even though some studies focused on improving the HER activity of Ni_3S_2 by nonmetal atoms doping [22,25,26], up to now, there are fewer investigations on modulating the OER activity of Ni_3S_2 by doping nonmetal atoms. Therefore, systematically investigating and rationally screening the nonmetal-atoms-doped Ni_3S_2 catalysts are needed to develop high performance OER electrocatalysts. Generally, it is time-consuming and of high cost to systematically screen the superior OER catalysts in experiments. Fortunately, with the help of high-performance computers and advanced theories of computational chemistry, we can screen the promising electrocatalysts at atomic scale by calculating the adsorption of intermediates, as well as reaction overpotentials, and further prepare the excellent catalysts by advanced experimental methods [1,23–25]. Thus, exploring the potential of nonmetal-atoms-doped Ni_3S_2 catalysts by combining theoretical prediction and experimental preparation to improve OER's catalytic activity can further develop the strategy for designing and constructing OER electrocatalysts.

Inspired by the above considerations, we systematically investigated the OER performances of five kinds of nonmetal-atoms (X, X = B, C, N, O, P)-doped Ni_3S_2 (X-Ni_3S_2) electrocatalysts and screened out the most promising X-Ni_3S_2 OER catalysts. The geometric and electronic structures of X-Ni_3S_2, intermediates adsorption, potential determining step (PDS), and theoretical overpotentials of OER were studied using the density functional theory (DFT) calculations. As a result, C can effectively disturb the local geometric and electronic structure of Ni_3S_2, thus adjusting the adsorption of key intermediates among all dopants, consequently enabling Ni_3S_2 to exhibit excellent OER performance with more active sites and much lower theoretical overpotentials. Additionally, C dopants can also improve the OER activity of nickel hydroxides when C-Ni_3S_2 incurs surface oxidation during the OER process. Guided by theoretical results, the C-Ni_3S_2 and Ni_3S_2 electrocatalysts with similar structure and morphology are synthesized in this work. C-Ni_3S_2 was verified to exhibit more optimized OER performance than Ni_3S_2 by means of electrochemical tests. Our theoretical prediction joins with experiment verification results provide a guide to designing promising catalysts for OER through nonmetal heteroatom doping engineering.

2. Computational Details

The periodic DFT calculations were carried out by employing the Vienna ab initio simulation package (VASP) [27]. The projector augmented wave (PAW) potentials [28] and the generalized gradient approximation (GGA) with the Perdew–Burke–Ernzerhof

(PBE) exchange-correlation functional [29] were used to describe electronic-ion interactions and model the electron exchange-correlation, respectively. A cutoff energy of 450 eV for plane-wave basis set, Monkhorst–Pack grid k-points of $3 \times 3 \times 1$, energy convergence criterion of 10^{-5} eV, and force convergence criterion of 0.02 eV/Å were employed for all slab models. When calculating the adsorption energy of intermediates, dipole corrections along the surface were considered, Van der Waals interactions were corrected by using Grimme's DFT-D3 method [30], and the solvent effect was included by using VASPsol [31].

The optimized Ni_3S_2 bulk [23] with rhombohedral crystal structure, lattice constant of 4.07 Å, Ni-S, and Ni-Ni bond lengths of 2.27 Å and 2.52 Å, respectively, all of which are very close to the experimental values [32]. As the (100) surface has the same atomic arrangement as that of the (001) and (010) surfaces and is the most studied and regarded as the most stable low-index surface with the lowest surface energy (Figure S1), the (100) surface was selected as the catalyst surface of Ni_3S_2 in the following investigations. The catalyst surface was simulated using a (2×2) $Ni_3S_2(100)$ slab cleaved from a Ni_3S_2 bulk cell. The dopant X includes B, C, N, O, and P, and all these X-Ni_3S_2 with 2.5 at% doping content (one of the S atoms in (2×2) $Ni_3S_2(100)$ slab containing 48 atoms was replaced by X atom) materials were validated with the possibility to be prepared in practice [23]. Furthermore, two types of X-$Ni_3S_2(100)$ surface models were constructed due to their similar surface stability, as our previous research mentioned [23]. They are X_{out}-$Ni_3S_2(100)$ and X_{in}-$Ni_3S_2(100)$, in which X substitutes one of the top-layer S atoms (X_{out}) and one of the sublayer S atoms (X_{in}) of $Ni_3S_2(100)$, respectively. Considering the surface oxidation and phase transition of Ni_3S_2 during the OER process [17,33], the (2×2) $Ni(OH)_2(100)$ and (2×2) NiOOH(100) surfaces were also constructed using the same method to verify the most effective dopant among those mentioned above. For all slab models, a 15 Å vacuum layer on the vertical direction of slab was added.

The key OER steps include the following:

$$H_2O + * \rightarrow *OH + H^+ + e^- \quad (1)$$

$$*OH \rightarrow *O + H^+ + e^- \quad (2)$$

$$*O + H_2O \rightarrow *OOH + H^+ + e^- \quad (3)$$

$$*OOH \rightarrow * + O_2 + H^+ + e^- \quad (4)$$

The free energies of each species were calculated according to the equation

$$G = E + ZPE - TS \quad (5)$$

where G, E, ZPE, and TS are the free energy, total energy, zero-point energy, and entropic contributions (T was set to be 300 K), respectively. ZPE and TS were calculated after obtaining the vibrational frequencies (v_i) [20]:

$$ZPE = \frac{1}{2}\sum h v_i \quad (6)$$

$$TS = k_B T[\sum ln\left(\frac{1}{1 - e^{-hv_i/k_B T}}\right) + \sum \frac{hv_i}{k_B T}\frac{1}{\left(e^{hv_i/k_B T} - 1\right)} + 1] \quad (7)$$

Here, the free energy of H^+ (G_{H^+}) can be regarded as $G_{H^+} = \frac{1}{2}G_{H_2}$, and the electrochemical potential of electron (G_e) is equal to $-eU$, where U is electrode potential relative to the reversible hydrogen electrode (RHE). Due to the inaccuracy of DFT in estimating the energy of O_2, the free energy of O_2 was derived according to $G_{O_2} = 2G_{H_2O} - 2G_{H_2} + 4.92$ eV [34]. The adsorption Gibbs free energy of main intermediates were calculated as follows:

$$\Delta G_{*OH} = G_{*OH} + \frac{1}{2}G_{H_2} - G_* - G_{*H_2O} \quad (8)$$

$$\Delta G_{*O} = G_{*O} + G_{H_2} - G_* - G_{*H_2O} \quad (9)$$

$$\Delta G_{*OOH} = G_{*OOH} + \frac{3}{2}G_{H_2} - G_{*} - 2G_{*H_2O} \quad (10)$$

Correspondingly, the Gibbs free energy of Equations (1)–(4) were calculated as follow:

$$\Delta G = \Delta E + \Delta ZPE - T\Delta S - eU \quad (11)$$

To evaluate the OER performance, the theoretical overpotential (η) is defined as

$$\eta = (\Delta G_{max})/e - 1.23\ \mathrm{V} \quad (12)$$

where ΔG_{max} is the most positive value from ΔG_1 to ΔG_4.

Experimental details can be found in Supplementary Materials.

3. Results and Discussion

3.1. The Local Geometric Environment and Electronic Structure of X-Ni_3S_2

Our previous work has validated that X-Ni_3S_2 can be prepared in experimental conditions, and the topmost layer and sublayer doping on Ni_3S_2(100) (X_{out}-Ni_3S_2(100) and X_{in}-Ni_3S_2(100), respectively) show good surface stability and might coexist due to the small difference in surface energy between them [23]. In addition, X-Ni_3S_2 shows good electronic conductivity because the orbitals cross the Fermi level shown in the density of states (DOS) of Ni_3S_2 with 2.5 at% X doping content (Figure S2). X-Ni_3S_2 can be a candidate for OER electrocatalysts, which can benefit the charge transfer between the surface and the intermediates during electrocatalysis [35].

In Figure 1a, the stable top-most Ni-nonmetal atomic arrangement of each surface denotes that X doping can well maintain the original ordered crystal structure of Ni_3S_2(100). While due to the radius (R_x) and electronegativity(χ_x) of X are different from those of S, X doping induces disturbance on local structure of surface. Clearly, the distance between X and Ni1 atoms ($d_{X\text{-}Ni1}$, Ni1 represents the nearest Ni atoms and labeled in Figure 1a) is different from the original $d_{S\text{-}Ni1}$. As shown in Figure 1b, except for the P-Ni1 bond, the other X-Ni1 bonds are shorter than the S-Ni1 bond. Additionally, C- and N-Ni_3S_2(100) surfaces have the shortest $d_{X\text{-}Ni1}$ than other X-Ni_3S_2(100) surfaces due to C and N having larger χ_x and smaller R_x. Interestingly, though the O atom has the smallest Rx and largest χ_x, the O-Ni1 bond is longer than the C-Ni1 and N-Ni1 bonds. This may be because O tends to form lone pair electrons when it bonds with the nearest metal atoms [24], which keeps it from getting any closer to Ni atoms. Moreover, the Ni1-Ni5 bonds (both Ni1 and Ni5 connect with X, Figure 1a) are also shorter than those on the pristine Ni_3S_2(100) surface (Table S1) due to the change of X-Ni1 bond. The change of X-Ni1 bond directly induces the change of adjacent Ni-Ni bond length, which further affects the bond length of adjacent Ni-S and distance between top-most Ni atoms. For example, the shorter C/N-Ni1 bond causes obviously shrinkage in the Ni1-Ni5 bond, which further elongates the Ni1-S3 and Ni5-S2 bonds, finally causing the slight displacement of topmost Ni atoms. Especially, among all X atoms, C and N cause more obvious changes in local Ni-Ni and Ni-S bond lengths, denoting that they can trigger prominent local structure disturbance on the Ni_3S_2(100) surface.

The local geometric structure was disturbed by the change of local coordination environment, which could be accompanied by changes in local electronic structure. Following this, the charges of surface atoms were calculated by Bader charge analysis [36] to examine the alteration of X on the electronic structure of the surface. As shown in Figure 1c, for all surfaces, the Ni1 atom which was directly affected by X possesses a positive charge (Q_{Ni1}), while X shows a negative charge (Q_X), denoting the Ni atoms deliver the charge to X atoms. Notably, compared with Q_{Ni1} of pristine Ni_3S_2(100), Q_{Ni1} is altered by X, and X with larger χ_x results in a more positive Q_{Ni1}. This charge transfer between X and Ni and the above-mentioned local structure change further affect the charge of adjacent S atoms (Figure 1d). For example, after C_{out} doping, a shorter C-Ni1 bond than the pristine S-Ni1 bond combines with more charge transfer between C and Ni1 than S and Ni1, resulting in the adjacent S (S3 atom in Figure 1a) atom bonding more strongly with sublayer Ni atoms

(Figure S3); thus, it has slightly more charge than the corresponding S atom on Ni_3S_2(100). Furthermore, the charges of surface Ni sites (i.e., top-most four Ni atoms, Ni1, Ni2, Ni3, and Ni4 in Figure 1a) are also disturbed by the change of local coordination environment. As shown in Figure 1d, on one X-Ni_3S_2(100) surface, Q_{Ni1} and Q_{Ni3} sites are intensely altered, accompanied by Q_{Ni2} and Q_{Ni4} being slightly altered by X, resulting in the four Ni sites having different charges. For example, Q_{Ni1}, Q_{Ni2}, Q_{Ni3}, and Q_{Ni4} of C_{out}-Ni_3S_2(100) are 0.46e, 0.48e, 0.43e, and 0.39e respectively, which are about 0.01~0.07e more positive than Q_{Ni1} of Ni_3S_2(100), indicating C dopants play a major role in alteration of electronic structure of Ni sites. Thus, according to above analysis, X dopants on Ni_3S_2(100) surface can disturb local geometric structure, change the charge distribution of surface, and modify the charge of Ni sites to varying degrees, which could further affect the OER intermediates' adsorption performance and consequently modify the OER activity on Ni_3S_2(100).

3.2. The OER Activity of X-Ni_3S_2(100)

We further probe into the OER activity of X-Ni_3S_2(100) to screen the promising X-Ni_3S_2 catalysts. For OER, the *OH, *O, and *OOH are key intermediates for elementary reactions (Equations (1)–(4)) on nickel-based sulfide [37]. To evaluate the OER activity of the pristine Ni_3S_2 surface, the adsorption of the above intermediates and free energy change (ΔG) of each elementary step on the pristine Ni_3S_2(100) surface were calculated, respectively, to recognize the adsorption site and the potential determining step (PDS) of OER. On pristine Ni_3S_2(100), *OH and *OOH tend to be absorbed on the Ni top site, while *O is likely to be absorbed on the Ni1-Ni2 bridge site as shown in Table S2; thus, the metal sites should be the reaction sites for OER. Accordingly, the OER pathway is illustrated in Figure 2a, and the free energy diagram is shown in Figure 2b. Apparently, all steps run uphill at U = 0 V vs. NHE and the third step, i.e., the *OOH formation (Equation (4)), is the PDS. This generates the highest ΔG of about 1.95 eV among four steps, corresponding to a theoretical overpotential (η) value of 0.72 V (or an onset potential value of 1.95 V), which is needed to make all steps of the free energy diagram go downhill. It means that the pristine Ni_3S_2(100) surface has a strong interaction with *OH and *O or too weak binding with *OOH. This is consistent with how the metal usually possesses a strong bonding interaction with *OH and *O [38]. Thus, it is deduced that properly weakening *O or OH* adsorption or strengthening *OOH binding would reduce the η and enhance the OER performance.

Further, we calculated the OER activity on X-Ni_3S_2. We first focused on the OER activity of Ni1 site, as it is directly bonded with X. Similar to the intermediate adsorption on the pristine Ni_3S_2(100) surface, the *OH, *O, and *OOH adsorbed on the Ni1 top, Ni1-Ni2 bridge, and Ni1 top sites, respectively. The free energy diagrams of the OER steps on the Ni1 site of X_{out} and X_{in}-Ni_3S_2(100) are shown in Figure 2c,d, respectively. For X_{out}-Ni_3S_2(100), all X dopants enhanced the *OH and *OOH adsorption, and B, C, and N enhanced the O adsorption, while O and P doping slightly weakened the O adsorption. This maintains the third step as the PDS, and the ΔG of PDS follows the trend of O > B > C > P > S > N (S represents pristine Ni_3S_2(100)), with the η trend of O (0.56 V) > B (0.61 V) > C (0.66 V) > P (0.67 V) > S (0.72 V) > N (0.80 V). Thus, except for N, all other X_{out} doping can enhance the OER activity on the Ni1 site of Ni_3S_2(100), especially the O_{out} doping, which almost enhances the OER activity on the Ni1 site by reducing η by 0.16 V compared with Ni_3S_2(100).

For X_{in}-Ni_3S_2(100), except B and P which weakened OH and OOH adsorption, all other X dopants enhanced the OH and OOH adsorption, and except C which weakened O adsorption, all other X dopants strengthened O adsorption. The PDS on the Ni1 site of X_{in}-Ni_3S_2(100) is still the *OOH formation step. The ΔG of PDS follows the trend of C > S > P > N > O > B, with the overpotential trend of C (0.49 V) > S (0.72 V) > P (0.96 V) > N (1.00 V) > O (1.03 V) > B (1.09 V). Thus, only C_{in} doping can enhance the OER activity on Ni1 site by reducing η by 0.23 V compared with Ni_3S_2(100), while other X_{in} doping may hinder the OER activity on the Ni1 site. According to the OER activity on the Ni1 site of both X_{out}- and X_{in}-Ni_3S_2(100), C dopant is beneficial for improving the OER activity of its

neighbor Ni site, while other X atoms enhance the OER activity of their neighbor Ni site only when doped at the topmost S site. As X_{in} and X_{out} may coexist in physical catalysts, the promising X-Ni_3S_2 catalysts should satisfy that both X_{in}-doped Ni_3S_2 and X_{out}-doped Ni_3S_2 have better OER activity than pristine Ni_3S_2. In this condition, the C dopant should be a good candidate for doping on the $Ni_3S_2(100)$ surface due to how both C_{in} and C_{out} can enhance the OER activity of their adjacent Ni sites.

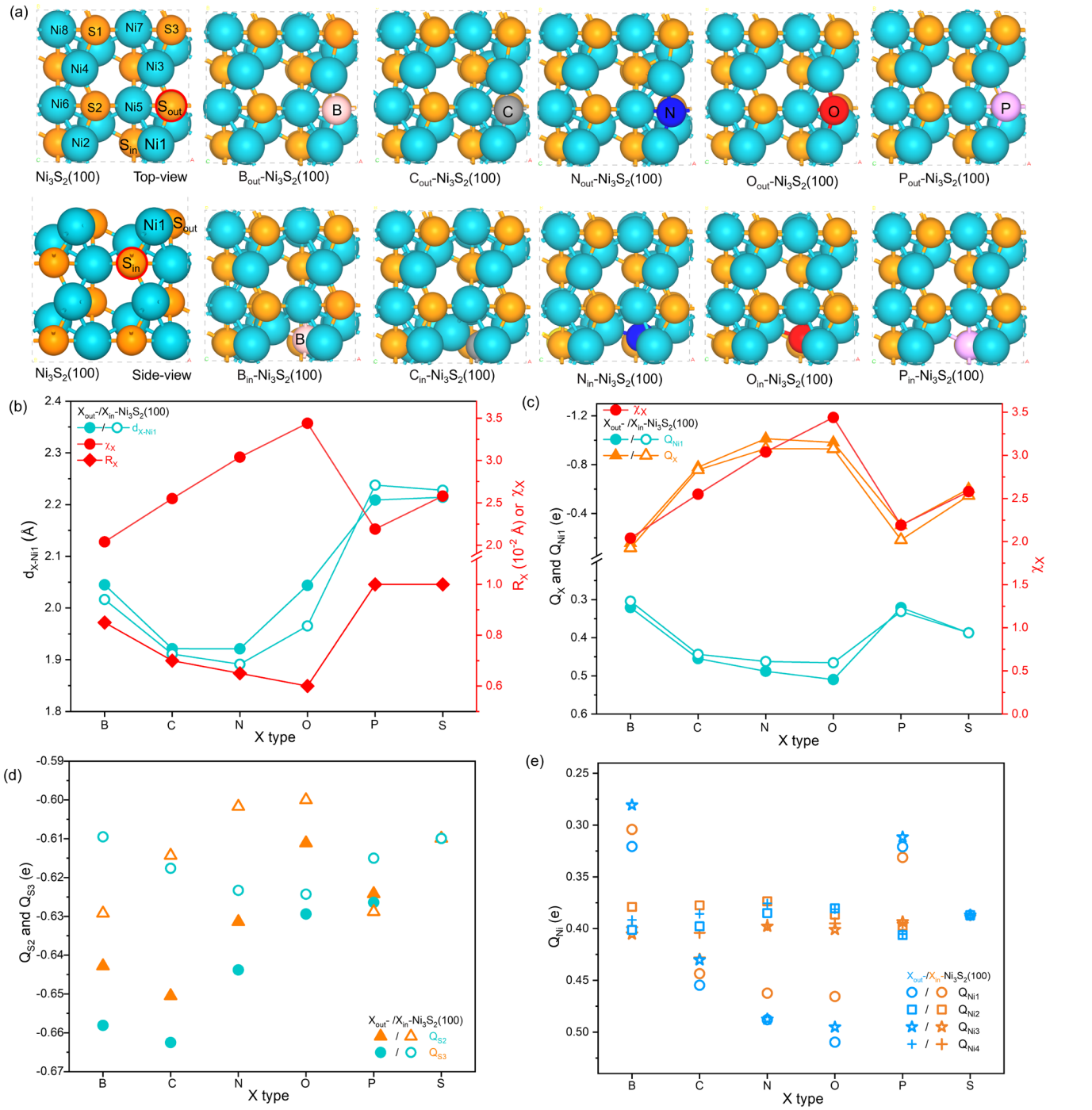

Figure 1. (**a**) The structures of $Ni_3S_2(100)$, X_{out}-$Ni_3S_2(100)$, and X_{in}-$Ni_3S_2(100)$ (surface Ni atoms are labeled as Ni1~Ni8, and Ni1~Ni4 represent top most Ni atoms, Ni5~Ni8 represent sublayer Ni atoms). (**b**) The bond length of X-Ni1 ($d_{X\text{-}Ni1}$) corelates with the electronegativity (χ_X) and atom radius (R_X) of X (S on horizontal axis represent pristine $Ni_3S_2(100)$). (**c**) Bader charge of Ni1(Q_{Ni1}) and X(Q_X) correlate with χ_X for both X_{out}-$Ni_3S_2(100)$ and X_{in}-$Ni_3S_2(100)$ systems. (**d**) The Bader charge of S2 and S3 atoms. (**e**) The Bader charge of Ni1~Ni4 atoms.

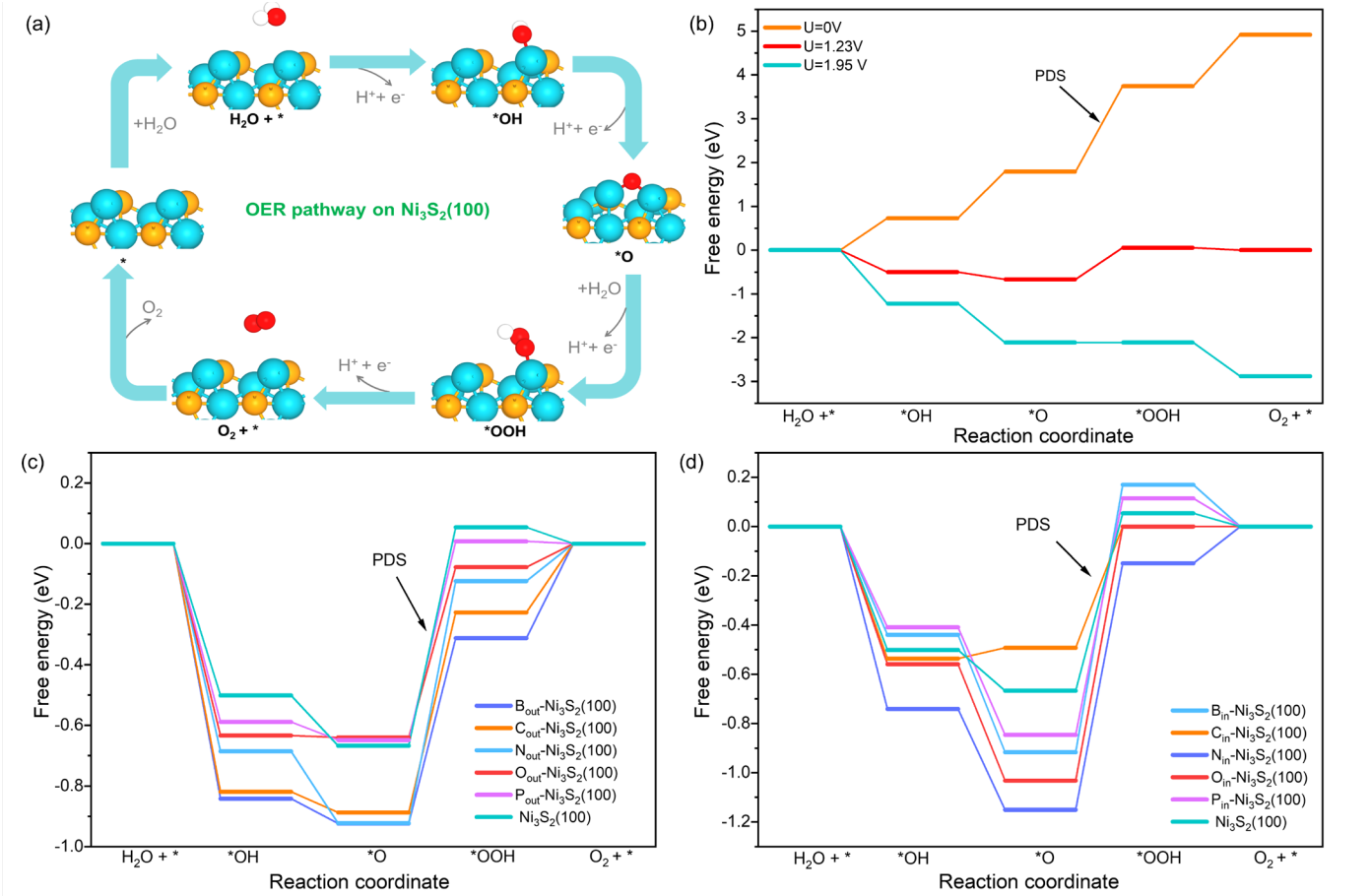

Figure 2. (**a**) The OER process on Ni site of $Ni_3S_2(100)$. (**b**–**d**) Free energy diagrams of OER on Ni1 site of $Ni_3S_2(100)$, X_{out}-$Ni_3S_2(100)$, and X_{in}-$Ni_3S_2(100)$, respectively. (* means surface active site).

On both X_{out}- and X_{in}-$Ni_3S_2(100)$ surfaces, Ni1 sites are directly affected by X, exhibiting different OER activity from that on pristine $Ni_3S_2(100)$. Considering that the surface geometric and electronic structure are disturbed by X dopants as discussed in Section 3.1, the intermediates' adsorption, and hence OER activity, on other Ni sites (Ni2, Ni3, and Ni4) may also be affected by X. Correspondingly, other Ni sites have the potential be more efficient OER active sites. Thus, OER activity on other Ni sites of each surface should be calculated and the number of efficient active sites needs to be counted to better screen out the most effective X dopants. Nevertheless, the adsorption of *O tends to coordinate with more metal atoms and has more complicated adsorption sites than *OH and *OOH (Figure S4 and Table S3), which make the calculation and screening of the effective adsorption site for OER intermediates too complex and high-cost. Usually, the adsorption free energy of *OH (ΔG_{*OH}) can be scaled, correlated with that of *OOH (ΔG_{*OOH}) on the same site [39,40]. Thus, it is possible to conveniently estimate the OER activity of different sites on X-$Ni_3S_2(100)$ by calculating the difference between the adsorption energy of *OOH or *OH and *O (ΔG_{*O}). Based on this, the relationship between ΔG_{*OH} and ΔG_{*OOH} on Ni1 sites of all X-$Ni_3S_2(100)$ were tested. As shown in Figure 3a, the larger ΔG_{*OH} corresponds to larger ΔG_{*OOH}, validating the linear scaling relation between ΔG_{*OH} and ΔG_{*OOH}, which follows the equation of

$$\Delta G_{*OOH} = \Delta G_{*OH} + 3.02 \text{ eV} \quad (13)$$

Thus, the sum free energy change of the second and third steps is fixed, that is

$$\Delta G_5 + \Delta G_6 = \Delta G_{*OOH} - \Delta G_{*OH} = 3.02 \text{ eV} \quad (14)$$

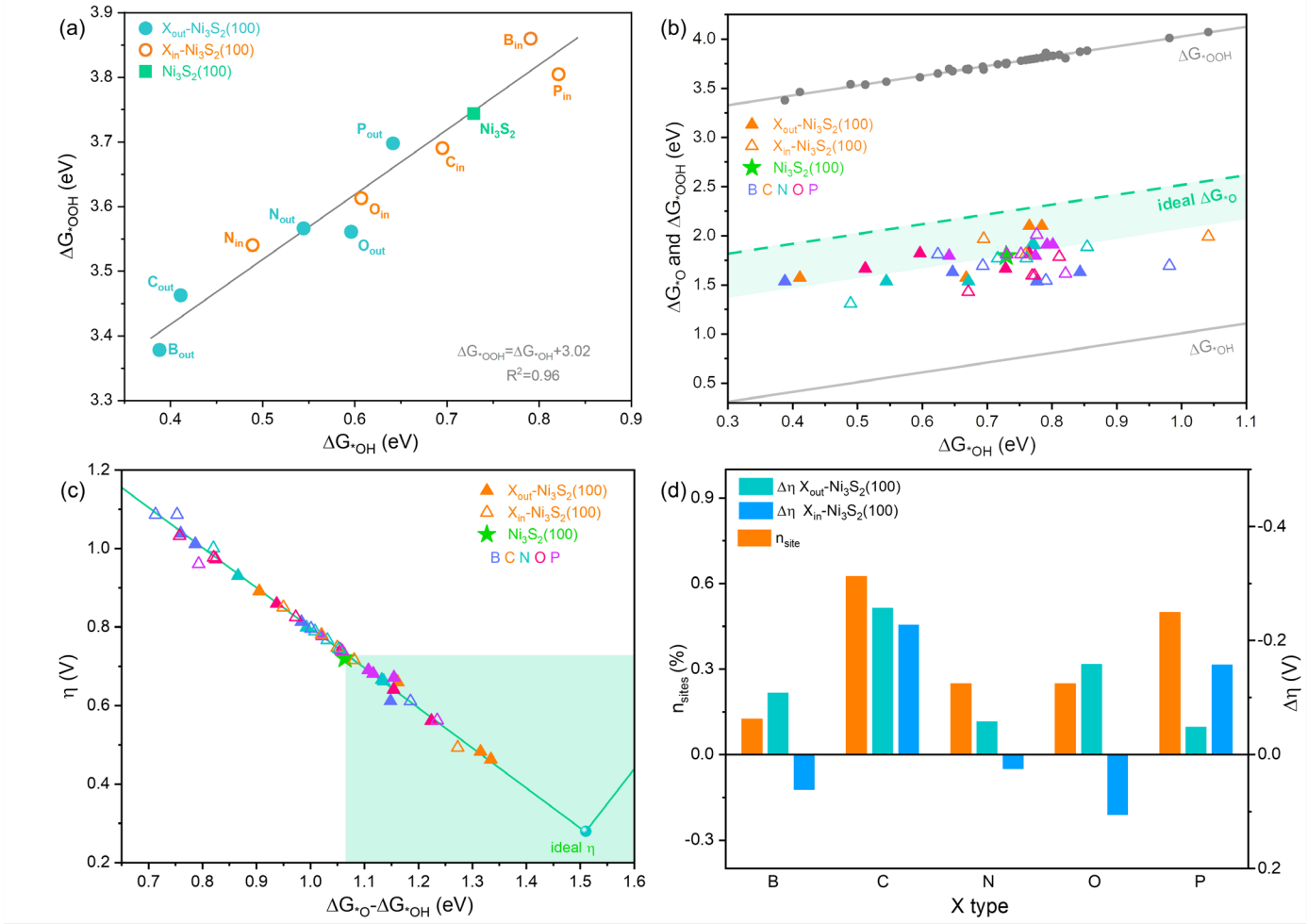

Figure 3. (**a**) The scale relation between ΔG_{*OH} and ΔG_{*OOH}. (**b**) The correlation between ΔG_{*O} (or ΔG_{*OOH}) and ΔG_{*OH}, and (**c**) the η vs. value of $\Delta G_{*O} - \Delta G_{*OH}$ on different X-Ni_3S_2(100) surfaces (the highlighted area in (**b**) and (**c**) denote the relative optimum ΔG_{*O} and small η values of X-Ni_3S_2(100), respectively). (**d**) The improved active site proportion (nsite) on X-Ni_3S_2(100) and the difference between minimum η of each surface and η of Ni_3S_2(100).

Hence, we can deduce that when ΔG_{*O} is in the middle of these two adsorption energies, that is, $\Delta G_{*O} - \Delta G_{*OH}$ or $\Delta G_{*OOH} - \Delta G_{*O}$ equals to the critical value of 1.51 eV, the lowest η of about 0.28 V for OER is obtained. Therefore, it suggests that the value of $\Delta G_{*O} - \Delta G_{*OH}$ or $\Delta G_{*OOH} - \Delta G_{*O}$ could be used as a descriptor to evaluate the OER activity. If the difference value of $\Delta G_{*O} - \Delta G_{*OH}$ is smaller than the critical value, the formation of *OOH is the PDS, such as that on pristine Ni_3S_2(100), and the η at standard conditions is

$$\eta = (\Delta G_{*O} - \Delta G_{*OH})/e - 1.23\ \text{V} \quad (15)$$

Conversely, if the difference value of $\Delta G_{*O} - \Delta G_{*OH}$ is larger than the critical value, the formation of *O (the second step) becomes the PDS, and the theoretical overpotential at standard conditions is

$$\eta = [3.02 - (\Delta G_{*O} - \Delta G_{*OH})]/e - 1.23\ \text{V} \quad (16)$$

Accordingly, all possible ΔG_{*OH} and corresponding ΔG_{*O} on X-Ni_3S_2(100) were calculated thoroughly (*OH on top sites, and *O on bridge sites shown in Figure S4) to evaluate the OER activity more accurately. The corresponding ΔG_{*OOH} was calculated using the linear scaling equation of ΔG_{*OH}. Figure 3b presents the location of ΔG_{*O}, and the difference value between ΔG_{*O} and ΔG_{*OH}. All ΔG_{*O} on X-Ni_3S_2(100) are close to the ΔG_{*OH},

denoting that the *OOH formation is still the PDS on pristine Ni_3S_2(100). Though the *O adsorption strength on X-Ni_3S_2(100) is a little stronger compared to the ideal *O adsorption strength, there are still many active sites showing weaker ΔG_{*O} on X-Ni_3S_2(100) than on pristine Ni_3S_2(100), indicating a possible higher OER activity of the former. The relationship between $\Delta G_{*O} - \Delta G_{*OH}$ and η is further plotted to confirm how many active sites of X-Ni_3S_2(100) have higher OER activity than pristine Ni_3S_2(100). In Figure 3c, there are 1, 5, 2, 2, and 4 of 8 sites on B-, C-, N, O-, and P-Ni_3S_2(100), respectively that have lower η than that of pristine Ni_3S_2(100), meaning that all X dopants can activate at least one surface Ni site, and C dopant contributes to the most active sites among five dopants. Moreover, the proportion of improved active site (n_{site}) and change value of η (Δη, more negative value means better activity than pristine Ni_3S_2(100)) on the best active site of each X-Ni_3S_2(100) are listed in Figure 3d. The n_{site} follow the sequence of C (62.5%) > P (50.0%) > O = N (25%) > B (12.5%), and Δη follows P_{out} (−0.05 V) > N_{out} (−0.06 V) > B_{out} (−0.11 V) > O_{out} (−0.16 V) > C_{out} (−0.26 V), and O_{in} (0.11 V) > B_{in} (0.06 V) > N_{in} (0.02 V) > P_{in} (−0.16 V) > C_{in} (−0.23 V) for X_{out}-Ni_3S_2(100) and X_{out}-Ni_3S_2(100), respectively. These values indicate that C is prominent among all dopants, can efficiently alter the OER active site and activate 62.5% of the surface Ni sites, and enable best active sites of both C_{out}- and C_{in}-Ni_3S_2(100) which have a much lower η relative to η of Ni_3S_2(100). Especially, C_{out} doping endows the surface with the lowest η of 0.46 V (Figure 3c), which is even comparable to 0.37 V of RuO_2 [41] and 0.51 V of IrO_2 [42]. Thus, considering both the number of active sites and activity of the Ni site, the C dopant can effectively activate the surface OER active site and can be selected as most effective dopant for X-Ni_3S_2 OER catalysts among all X dopants.

Furthermore, considering the surface oxidation and phase transition of Ni_3S_2 to exist as Ni-based hydroxides (such as $Ni(OH)_2$ and NiOOH) during OER processes [17,33], and to further verify the efficiency of the promising C dopant, we evaluated the OER activity of C-doped Ni-based hydroxides (the adsorption structures are shown in Figure S5). As shown in Figure S6a,b, when C is doped on both $Ni(OH)_2$ and NiOOH, it can enhance the adsorption of OER intermediates, which is especially beneficial to the O adsorption. Consequently, the decrease the free energy of the PDS generates the η of 0.07 and 0.13 V lower than those of pristine $Ni(OH)_2$ and NiOOH, respectively. Thus, C dopants not only help to improve the OER activity of pristine Ni_3S_2 but also contribute to the OER activity of Ni-based hydroxides, denoting that C-Ni_3S_2 can serve as a promising OER electrocatalyst.

Based on these theoretical prediction results, the C-doped Ni_3S_2 nanosheets (C-Ni_3S_2 NSs), as well as Ni_3S_2 nanosheets (Ni_3S_2 NSs), were synthesized in the same way used in previous study [23] (also see Supplementary Matrials for more detail) to verify its application in OER. Our previous work has demonstrated that C-Ni_3S_2 NSs and pristine Ni_3S_2 NSs have similar nanosheet morphology and the same crystal structure and uniform elemental distribution. Thus, we mainly focused on studying the OER performance of these two samples in this study. The OER activities of samples were evaluated in 1 M KOH. Figure 4a,b shows the LSV of the above samples and a comparison of their catalytic activities for OER, respectively. The C-Ni_3S_2 NSs exhibit higher OER activity than pristine Ni_3S_2 NSs, needing a lower overpotential of 261 mV and 480 mV to reach current density of 10 mA cm^{-2} and 900 mA cm^{-2}, respectively, compared with Ni_3S_2 NSs (310 mV, 590 mV, respectively). The corresponding Tafel slope (Figure S7a) of C-Ni_3S_2 NSs (96.18 mV dec^{-1}) is lower than that of pristine Ni_3S_2 NSs (109.35 mV dec^{-1}), indicating the favorable reaction kinetics of C-Ni_3S_2 NSs. Nyquist plots in Figure S7b illustrate that C-Ni_3S_2 NSs have faster charge transfers between electrolyte and electrode. Furthermore, C-Ni_3S_2 NSs also show higher exchange current density (J_0) (Figures 4b and S7c) and average turnover frequency (TOF) of 0.02 mA cm^{-2} and 0.31, respectively, than those of Ni_3S_2 NSs (0.02 mA cm^{-2} and 0.06, respectively). Additionally, C-Ni_3S_2 NSs exhibits similar electrochemical double-layer capacitance with that of Ni_3S_2 NSs (Figure S7d). Moreover, the OER activity of the as-prepared catalyst is comparable to that of most reported nickel-based OER catalysts (Table S4).These experimental results validate that the C-Ni_3S_2 NSs have improved OER

performance compared with pristine Ni_3S_2 NSs, which is in line with the above DFT results, highlighting the effectiveness of C dopant modification in the OER activity of Ni_3S_2.

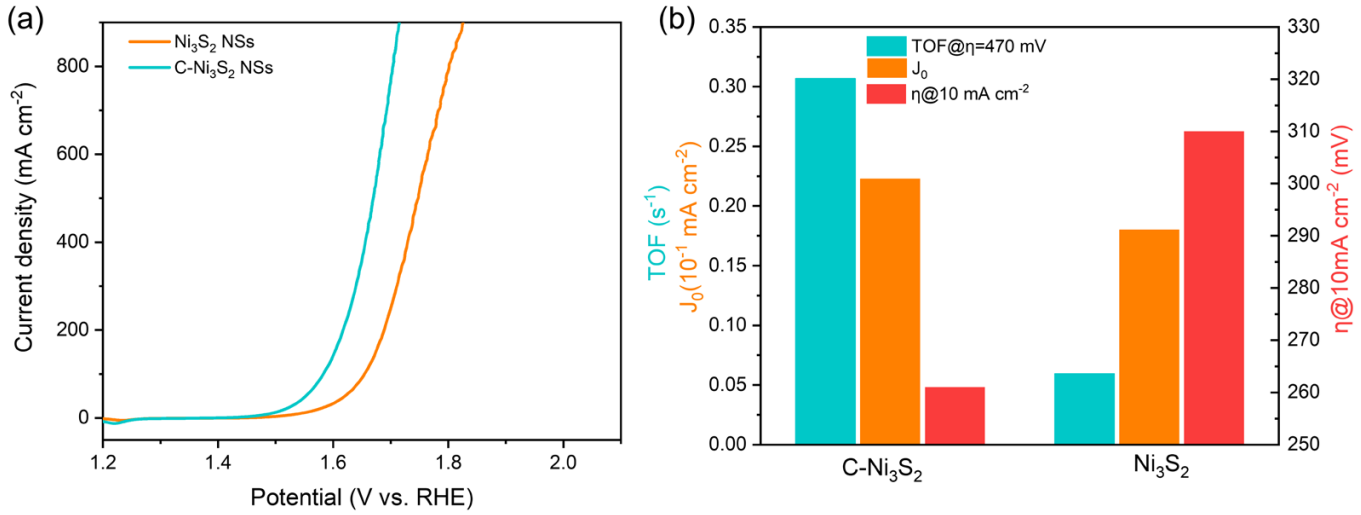

Figure 4. (**a**) The OER polarization curves and (**b**) overpotential (η) at current density of 10 mA cm^{-2}, average turnover frequency (TOF), and exchange current density (J_0) of Ni_3S_2 NSs and X-Ni_3S_2 NSs electrocatalysts.

3.3. The Origin of Improved OER Activity of C-Doped Ni_3S_2(100)

For further insight into the improved OER activity of C-doped Ni_3S_2(100), the geometric and electronic structure of key OER intermediates on the most effective site, i.e., the Ni3 site of C_{out}-Ni_3S_2(100), were discussed as an example. As shown in Figure S8, for OH and OOH, they both adsorbed on the Ni3 top site to form a single O-Ni bond, and the bond length of all O-Ni bonds on C_{out}-Ni_3S_2(100) are longer than that on Ni_3S_2(100). The charge density difference displayed in Figure 5a shows O of *OH or *OOH can acquire charge through O-Ni bods, due to how charge can transfer from Ni to O and some charge can also transfer from C and S to O through Ni. The Bader charge in Figure 5a indicates that O of *OH or *OOH acquires less charge from the Ni3 site of C_{out}-Ni_3S_2(100) than from the Ni site of Ni_3S_2(100). Furthermore, the DOS of the O-Ni atoms pair in *OH shown in Figure 4b display that the main states below fermi level (−3.0~−4.5 eV) of the O atom on C_{out}-Ni_3S_2(100) are slightly less than that of the O atom on Ni_3S_2(100), verifying less charge transfer from the Ni3 site of C_{out}-Ni_3S_2(100) to *OH/*OOH. Thus, the C dopant can slightly elongate the O-Ni3 bond and decrease the charge transfer from Ni3 to O, consequently helping to impair the O-Ni3 interaction and weaken the OH and OOH adsorption (Figure 4c). For *O adsorption on Ni3 of C_{out}-Ni_3S_2(100), it tends to bond with Ni3 and the sublayer Ni atom (Ni7 in Figure 1a), forming two Ni-O bonds after optimization, which are different from those of *O bonds with the topmost two Ni atoms (Ni3 and Ni4) on Ni_3S_2(100). This makes the average Ni-O bond of *O on C_{out}-Ni_3S_2(100) longer than that of *O on Ni_3S_2(100), and *O acquires less charge from Ni (Ni3 and Ni7) of C_{out}-Ni_3S_2(100) than from Ni (Ni3 and Ni4) of Ni_3S_2(100) (Figure 5a). Furthermore, the states below Fermi level of O on C_{out}-Ni_3S_2(100) are less than that of *O on Ni_3S_2(100), manifesting the lower charge transfer between O-Ni. More importantly, the electronic states interaction between O and Ni of C_{out}-Ni_3S_2(100) occur at a higher energy level than that of Ni_3S_2(100), confirming the weaker O-Ni interaction, and consequently, the weaker *O adsorption on the Ni3 site of C_{out}-Ni_3S_2(100) than that on the Ni site of Ni_3S_2(100).

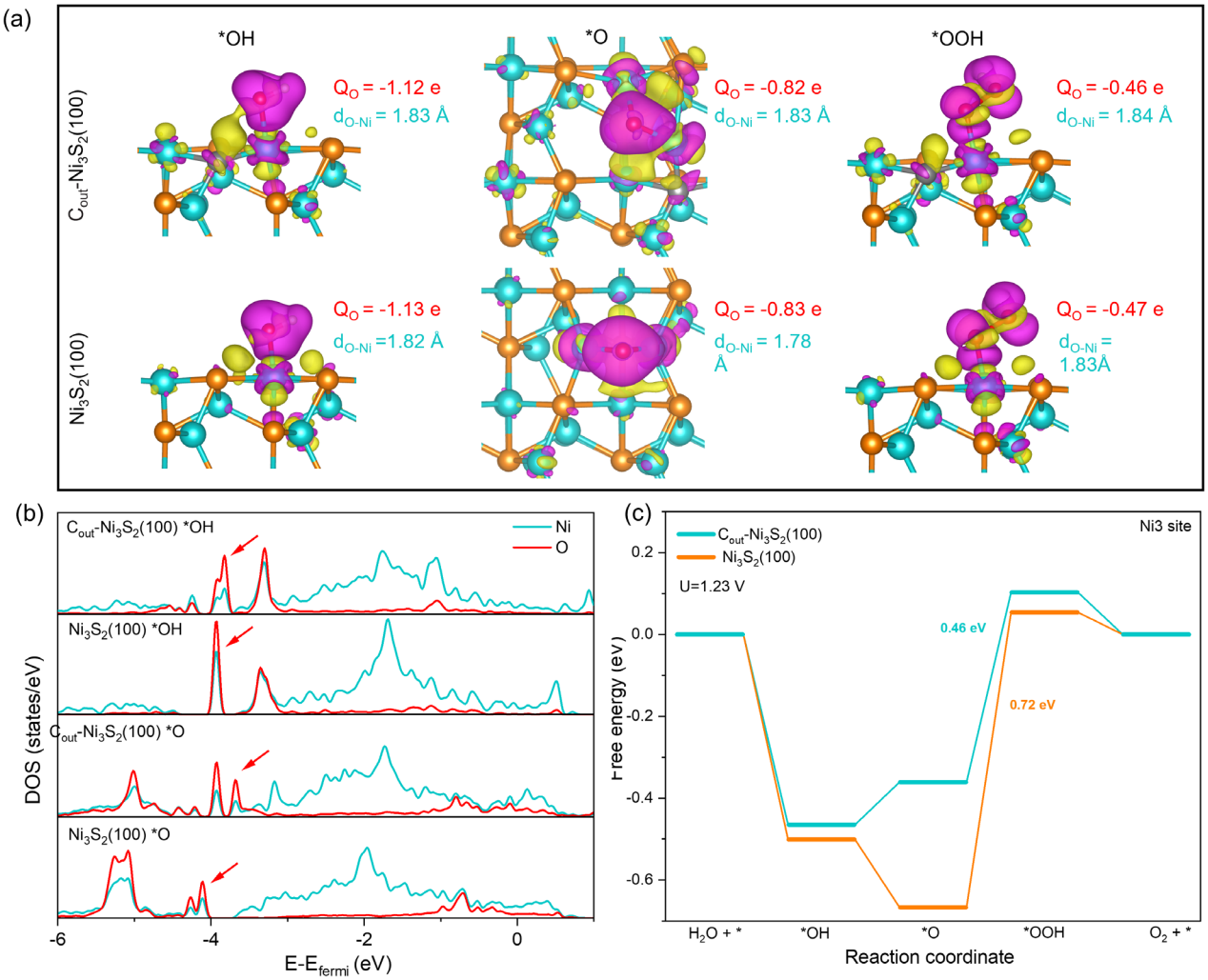

Figure 5. (**a**) The Bader charge of O (Q_{Ni}), bond legth of O-Ni (d_{O-Ni}), and the charge density difference of OER intermediates adsorption on Ni3 site of C_{out}-Ni_3S_2(100) and Ni site of Ni_3S_2(100) (The purple part represents charge accumulation, while yellow part represents charge depletion. The isosurface level is set as 0.002 eV $Å^{-3}$). (**b**) The density of states (DOS) for OH and O adsorption on the Ni3 site of C_{out}-Ni_3S_2(100) and Ni site of Ni_3S_2(100). (**c**) The OER free energy diagram of Ni3 site of C_{out}-Ni_3S_2(100) and Ni site of Ni_3S_2(100).

The weakened OER intermediate adsorption on the Ni3 site of C_{out}-Ni_3S_2(100) mainly results from an electronic structure alerted by C dopants. C dopant makes the charge of Ni3 site more positive and the d band center of Ni3 site negatively shift when compared with those of the Ni site on Ni_3S_2(100) (Table S5). Consequently, this decreases the charge transferred from Ni to O and weakens the O-Ni bonds. Moreover, the surface structure also contributes to weakening the O adsorption. Specifically, the disturbance on local structure caused by C_{out} makes the Ni3-Ni4 distance (4.68 Å) longer than the pristine Ni3-Ni4 distance (4.07 Å), which leads O to prefer bonding with Ni3 and the Ni7 atoms rather than Ni4 atom. Due to the more saturated coordination and lower position in the Z direction of the Ni4 atom, O forms a longer and weaker Ni-O bond with the Ni atom. Thus, the special surface geometric and electronic structure induced by C doping can weaken OER intermediates' (especially O) adsorption on the Ni3 site of C_{out}-Ni_3S_2(100) and reduce the ΔG of the PDS ($\Delta G_{*OOH} - \Delta G_{*O}$), consequently yielding a better OER activity with η as low as 0.46 V (Figure 5c).

4. Conclusions

In summary, the geometric structure, charge transfer, and OER activity of nonmetal atoms X (X = B, C, N, O, P)-doped Ni_3S_2 were studied systematically using DFT calculations. This demonstrated that the geometric structure and electronic structure, hence OER activity, are disturbed by the introduction of X dopants. Among all X dopants, C can be a promising dopant for Ni_3S_2 materials due to the way it can efficiently alter the local geometric structure and electronic structure of the Ni site, hence adjusting the key intermediates adsorption. This consequently enables the modified Ni_3S_2(100) surface to have the most effective active sites and exhibits the best OER activity, with the lowest theoretical overpotential of 0.46 V, which is 0.26 V lower than that of pristine Ni_3S_2(100). Further electrochemical experiments verified that C-doped Ni_3S_2 indeed presents higher intrinsic OER activity than pristine Ni_3S_2, which needs the 49 mV lower overpotential than that of pristine Ni_3S_2 to deliver a geometrical current density of 10 mA cm^{-2} in 1 M KOH. Above all, the DFT calculation and experimental results jointly highlight the promising C dopant in promoting the OER performance of Ni_3S_2. Our study offers guidance for screening and fabricating promising OER catalysts through nonmetal doping engineering, which can inspire more exploration of nonmetal doping of other electrocatalysts.

Supplementary Materials: The following supporting information can be downloaded at https://www.mdpi.com/article/10.3390/en16020881/s1. Figure S1. The surface energy (δ_S) of (100), (111) and (110) surfaces. (As the (001) and (010) have same structure as (100) and (101) has same structure as (110), we do not consider (001), (010) and (101) anymore. The δ_S is calculated according to $\delta_S = \frac{E_{(slab)} - N_{Ni}\mu_{Ni} - N_S\mu_S}{A}$, where $E_{(slab)}$ is the energy of slab, N_{Ni}, N_S and N_X represent the number of Ni, S and X atoms respectively, and A is the surface area of a slab). Figure S2. (a) The partial density of states for pure Ni_3S_2. (b) The total density of states for X doped Ni_3S_2(only half of DOS is displayed). Figure S3. the Bond length of S3-Ni and X-Ni bonds on C_{out}-Ni_3S_2(100) and Ni_3S_2(100). Figure S4. The adsorption site on (a) X_{out}-Ni_3S_2(100) surface or pristine Ni_3S_2(100) surface and (b) X_{in}-Ni_3S_2(100) surface. (Top sites are for OH or OOH adsorption, while bridge sites are for O adsorption). Figure S5. The structure of OER intermediats adsorption on prinstin and C doped $Ni(OH)_2$ and NiOOH. Figure S6. (a,b) Free energy diagram of OER on pristine and C doped $Ni(OH)_2$ and NiOOH respectively. Figure S7. (a) The Tafel slop, (b) Nyquist plots obtained by electrochemical impedance spectroscopy. (c) turnover frequency (TOF) and (d) electrochemical double-layer capacitance of C- Ni_3S_2 NSs and Ni_3S_2 NSs. Figure S8. The structures of OER intermediates on Ni3 site of C_{out}-Ni_3S_2(100) and pristine Ni_3S_2(100). Table S1. The bond length of X-Ni1 ($d_{X\text{-}Ni1}$) and Ni1-Ni5 ($d_{Ni1\text{-}Ni5}$) bonds, corresponding bonds length deviation after X doping ($\Delta d_{X\text{-}Ni1}$ and $\Delta d_{Ni1\text{-}Ni5}$, more nagetive value means shorter bond), electronegativity (χ_x) and atom radius (R_x) of X. Table S2. The adsorption free energy of OH, O and OOH on Ni_3S_2(100) surface. Table S3. The ΔG_{*OH} and ΔG_{*O} of C_{out}-Ni_3S_2(100) and C_{in}-Ni_3S_2(100) (as examples). Table S4. The comparison of OER activity between catalyst in this work and in recent works. Table S5. Bader charge and b band center of Ni3 site and Ni site of C_{out}-Ni_3S_2(100) and Ni_3S_2(100).

Author Contributions: Conceptualization, X.Z.; methodology, X.Z.; validation, L.Z.; data curation, W.H.; writing—original draft preparation, X.Z.; writing—review and editing, L.L. and S.L.; visualization, X.Z.; supervision, L.L.; funding acquisition, X.Z., L.L. and S.L. All authors have read and agreed to the published version of the manuscript.

Funding: This research was funded by the National Natural Science Foundation of China (No. 52200076), the National Key R&D Program (2021YFB4000301), the Research Foundation of Chongqing University of Science and Technology (Grant No. ckrc2022026), Natural Science Foundation of Chongqing (Grant No. CSTB2022NSCQ-BHX0035), Special Research Assistant Program of Chinese Academy of Science.

Data Availability Statement: Not applicable.

Conflicts of Interest: The authors declare no conflict of interest.

References

1. Babar, P.; Mahmood, J.; Maligal-Ganesh, R.V.; Kim, S.-J.; Xue, Z.; Yavuz, C.T. Electronic structure engineering for electrochemical water oxidation. *J. Mater. Chem. A* **2022**, *10*, 20218–20241. [CrossRef]
2. Lu, S.; Hummel, M.; Gu, Z.; Wang, Y.; Wang, K.; Pathak, R.; Zhou, Y.; Jia, H.; Qi, X.; Zhao, X.; et al. Highly efficient urea oxidation via nesting nano-nickel oxide in eggshell membrane-derived carbon. *ACS Sustain. Chem. Eng.* **2021**, *9*, 1703–1713. [CrossRef]
3. Reier, T.; Oezaslan, M.; Strasser, P. Electrocatalytic Oxygen Evolution Reaction (OER) on Ru, Ir, and Pt Catalysts: A Comparative Study of Nanoparticles and Bulk Materials. *ACS Catal.* **2012**, *2*, 1765–1772. [CrossRef]
4. Kwon, T.; Hwang, H.; Sa, Y.J.; Park, J.; Baik, H.; Joo, S.H.; Lee, K. Cobalt Assisted Synthesis of IrCu Hollow Octahedral Nanocages as Highly Active Electrocatalysts toward Oxygen Evolution Reaction. *Adv. Funct. Mater.* **2017**, *27*, 1604688. [CrossRef]
5. Lee, Y.; Suntivich, J.; May, K.J.; Perry, E.E.; Shao-Horn, Y. Synthesis and Activities of Rutile IrO_2 and RuO_2 Nanoparticles for Oxygen Evolution in Acid and Alkaline Solutions. *J. Phys. Chem. Lett.* **2012**, *3*, 399–404. [CrossRef]
6. Zhao, X.; Zhang, H.; Yan, Y.; Cao, J.; Li, X.; Zhou, S.; Peng, Z.; Zeng, J. Engineering the Electrical Conductivity of Lamellar Silver-Doped Cobalt(II) Selenide Nanobelts for Enhanced Oxygen Evolution. *Angew. Chem. Int. Ed. Engl.* **2017**, *56*, 328–332. [CrossRef]
7. Gu, C.; Hu, S.; Zheng, X.; Gao, M.R.; Zheng, Y.R.; Shi, L.; Gao, Q.; Zheng, X.; Chu, W.; Yao, H.B.; et al. Synthesis of Sub-2 nm Iron-Doped NiSe2 Nanowires and Their Surface-Confined Oxidation for Oxygen Evolution Catalysis. *Angew. Chem. Int. Ed. Engl.* **2018**, *57*, 4020–4024. [CrossRef] [PubMed]
8. Lu, S.; Hummel, M.; Gu, Z.; Gu, Y.; Cen, Z.; Wei, L.; Zhou, Y.; Zhang, C.; Yang, C. Trash to treasure: A novel chemical route to synthesis of NiO/C for hydrogen production. *Int. J. Hydrogen Energy* **2019**, *44*, 16144–16153. [CrossRef]
9. Yan, C.; Yang, X.; Lu, S.; Han, E.; Chen, G.; Zhang, Z.; Zhang, H.; He, Y. Hydrothermal synthesis of vanadium doped nickel sulfide nanoflower for high-performance supercapacitor. *J. Alloys Compd.* **2022**, *928*, 167189. [CrossRef]
10. Park, S.H.; Kang, S.H.; Youn, D.H. Direct One-Step Growth of Bimetallic Ni_2Mo_3N on Ni Foam as an Efficient Oxygen Evolution Electrocatalyst. *Materials* **2021**, *14*, 4768. [CrossRef]
11. Luo, X.; Ma, H.; Gao, J.; Yu, L.; Gu, X.; Liu, J. Nickel-Rich Ni_3N Particles Stimulated by Defective Graphitic Carbon Nitrides for the Effective Oxygen Evolution Reaction. *Ind. Eng. Chem. Res.* **2022**, *61*, 2081–2090. [CrossRef]
12. Wu, Z.-Y.; Ji, W.-B.; Hu, B.-C.; Liang, H.-W.; Xu, X.-X.; Yu, Z.-L.; Li, B.-Y.; Yu, S.-H. Partially oxidized Ni nanoparticles supported on Ni-N co-doped carbon nanofibers as bifunctional electrocatalysts for overall water splitting. *Nano Energy* **2018**, *51*, 286–293. [CrossRef]
13. Xia, B.; Wang, T.; Jiang, X.; Li, J.; Zhang, T.; Xi, P.; Gao, D.; Xue, D. N+-ion irradiation engineering towards the efficient oxygen evolution reaction on NiO nanosheet arrays. *J. Mater. Chem. A* **2019**, *7*, 4729–4733. [CrossRef]
14. Kim, B.K.; Kim, S.-K.; Cho, S.K.; Kim, J.J. Enhanced catalytic activity of electrodeposited Ni-Cu-P toward oxygen evolution reaction. *Appl. Catal. B* **2018**, *237*, 409–415. [CrossRef]
15. Wu, Y.; Li, G.-D.; Liu, Y.; Yang, L.; Lian, X.; Asefa, T.; Zou, X. Overall Water Splitting Catalyzed Efficiently by an Ultrathin Nanosheet-Built, Hollow Ni_3S_2-Based Electrocatalyst. *Adv. Funct. Mater.* **2016**, *26*, 4839–4847. [CrossRef]
16. Zhao, Y.; You, J.; Wang, L.; Bao, W.; Yao, R. Recent advances in Ni_3S_2-based electrocatalysts for oxygen evolution reaction. *Int. J. Hydrogen Energy* **2021**, *46*, 39146–39182. [CrossRef]
17. Ai, T.; Wang, H.; Bao, W.; Feng, L.; Zou, X.; Wei, X.; Ding, L.; Deng, Z.; Rao, B. Fe-V synergistic doping effect of hierarchical Ni_3S_2 oblate-nanorod arrays for efficient electrocatalytic oxygen evolution reaction. *Chem. Eng. J.* **2022**, *450*, 138358. [CrossRef]
18. Lu, S.; Wang, Y.; Xiang, H.; Lei, H.; Xu, B.B.; Xing, L.; Yu, E.H.; Liu, T.X. Mass transfer effect to electrochemical reduction of CO_2: Electrode, electrocatalyst and electrolyte. *J. Energy Storage* **2022**, *52*, 104764. [CrossRef]
19. Zhong, B.; Cheng, B.; Zhu, Y.; Ding, R.; Kuang, P.; Yu, J. Hierarchically porous nickel foam supported Fe-Ni_3S_2 electrode for high-current-density alkaline water splitting. *J. Colloid Interface Sci.* **2022**, *629*, 846–853. [CrossRef]
20. Liu, Q.; Xie, L.; Liu, Z.; Du, G.; Asiri, A.M.; Sun, X. A Zn-doped Ni_3S_2 nanosheet array as a high-performance electrochemical water oxidation catalyst in alkaline solution. *Chem. Commun.* **2017**, *53*, 12446–12449. [CrossRef]
21. Wang, H.-F.; Tang, C.; Li, B.-Q.; Zhang, Q. A review of anion-regulated multi-anion transition metal compounds for oxygen evolution electrocatalysis. *Inorg. Chem. Front.* **2018**, *5*, 521–534. [CrossRef]
22. Chen, P.; Zhou, T.; Zhang, M.; Tong, Y.; Zhong, C.; Zhang, N.; Zhang, L.; Wu, C.; Xie, Y. 3D Nitrogen-Anion-Decorated Nickel Sulfides for Highly Efficient Overall Water Splitting. *Adv. Mater.* **2017**, *29*, 1701584. [CrossRef] [PubMed]
23. Zheng, X.; Zhang, L.; Huang, J.; Peng, L.; Deng, M.; Li, L.; Li, J.; Chen, H.; Wei, Z. Boosting Hydrogen Evolution Reaction of Nickel Sulfides by Introducing Nonmetallic Dopants. *J. Phy. Chem. C* **2020**, *124*, 24223–24231. [CrossRef]
24. Zheng, X.Q.; Peng, L.S.; Li, L.; Yang, N.; Yang, Y.J.; Li, J.; Wang, J.C.; Wei, Z.D. Role of non-metallic atoms in enhancing the catalytic activity of nickel-based compounds for hydrogen evolution reaction. *Chem. Sci.* **2018**, *9*, 1822–1830. [CrossRef] [PubMed]
25. Zhong, X.; Tang, J.; Wang, J.; Shao, M.; Chai, J.; Wang, S.; Yang, M.; Yang, Y.; Wang, N.; Wang, S.; et al. 3D heterostructured pure and N-Doped Ni 3 S 2 /VS 2 nanosheets for high efficient overall water splitting. *Electrochim. Acta* **2018**, *269*, 55–61. [CrossRef]
26. Ding, Y.; Li, H.; Hou, Y. Phosphorus-doped nickel sulfides/nickel foam as electrode materials for electrocatalytic water splitting. *Int. J. Hydrogen Energy* **2018**, *43*, 19002–19009. [CrossRef]
27. Kresse, G.; Furthmuller, J. Efficient iterative schemes for ab initio total-energy calculations using a plane-wave basis set. *Phy. Rev. B* **1996**, *54*, 11169–11186. [CrossRef]
28. Blochl, P.E. Projector Augmented-Wave Method. *Phy. Rev. B* **1994**, *50*, 17953–17979. [CrossRef]

29. Perdew, J.P.; Burke, K.; Ernzerhof, M. Generalized gradient approximation made simple. *Phys. Rev. Lett.* **1996**, *77*, 3865–3868. [CrossRef]
30. Grimme, S.; Ehrlich, S.; Goerigk, L. Effect of the damping function in dispersion corrected density functional theory. *J. Comput. Chem.* **2011**, *32*, 1456–1465. [CrossRef]
31. Mathew, K.; Sundararaman, R.; Letchworth-Weaver, K.; Arias, T.A.; Hennig, R.G. Implicit solvation model for density-functional study of nanocrystal surfaces and reaction pathways. *J. Chem. Phys.* **2014**, *140*, 084106. [CrossRef] [PubMed]
32. Fleet, M.E. The crystal structure of heazlewoodite, and metallic bonds in sulfide mineral. *Am. Miner.* **1977**, *62*, 341–345.
33. Lu, S.; Hummel, M.; Kang, S.; Pathak, R.; He, W.; Qi, X.; Gu, Z. Density Functional Theory Investigation of the NiO@Graphene Composite as a Urea Oxidation Catalyst in the Alkaline Electrolyte. *ACS Omega* **2022**, *6*, 14648–14654. [CrossRef]
34. Peng, L.S.; Wang, J.; Nie, Y.; Xiong, K.; Wang, Y.; Zhang, L.; Chen, K.; Ding, W.; Li, L.; Wei, Z.D. Dual-Ligand Synergistic Modulation: A Satisfactory Strategy for Simultaneously Improving the Activity and Stability of Oxygen Evolution Electrocatalysts. *ACS Catal.* **2017**, *7*, 8184–8191. [CrossRef]
35. Ghadge, S.D.; Velikokhatnyi, O.I.; Datta, M.K.; Damodaran, K.; Shanthi, P.M.; Kumta, P.N. Highly Efficient Fluorine Doped Ni2P Electrocatalysts for Alkaline Mediated Oxygen Evolution Reaction. *J. Electrochem. Soc.* **2021**, *168*, 064512. [CrossRef]
36. Henkelman, G.; Arnaldsson, A.; Jónsson, H. A fast and robust algorithm for Bader decomposition of charge density. *Comput. Mater. Sci.* **2006**, *36*, 354–360. [CrossRef]
37. Feng, L.L.; Yu, G.; Wu, Y.; Li, G.D.; Li, H.; Sun, Y.; Asefa, T.; Chen, W.; Zou, X. High-index faceted Ni_3S_2 nanosheet arrays as highly active and ultrastable electrocatalysts for water splitting. *J. Am. Chem. Soc.* **2015**, *137*, 14023–14026. [CrossRef] [PubMed]
38. Rossmeisl, J.; Logadottir, A.; Nørskov, J.K. Electrolysis of water on (oxidized) metal surfaces. *Chem. Phys.* **2005**, *319*, 178–184. [CrossRef]
39. Back, S.; Jung, Y. Importance of Ligand Effects Breaking the Scaling Relation for Core-Shell Oxygen Reduction Catalysts. *Chemcatchem* **2017**, *9*, 3173–3179. [CrossRef]
40. Liang, W.; Chen, J.; Liu, Y.; Chen, S. Density-Functional-Theory Calculation Analysis of Active Sites for Four-Electron Reduction of O2on Fe/N-Doped Graphene. *ACS Catal.* **2014**, *4*, 4170–4177. [CrossRef]
41. Rossmeisl, J.; Qu, Z.W.; Zhu, H.; Kroes, G.J.; Nørskov, J.K. Electrolysis of water on oxide surfaces. *J. Electroanal. Chem.* **2007**, *607*, 83–89. [CrossRef]
42. Sun, W.; Song, Y.; Gong, X.Q.; Cao, L.M.; Yang, J. An efficiently tuned d-orbital occupation of IrO2 by doping with Cu for enhancing the oxygen evolution reaction activity. *Chem. Sci.* **2015**, *6*, 4993–4999. [CrossRef] [PubMed]